Ultra-Low Crosstalk and Fabrication-Tolerant Silicon-Nitride O-Band (de)Multiplexer Using Bragg Grating-Assisted Contra-Directional Coupler

Kuo-Fang Chung, Tien-Tsorng Shih, *Member, IEEE*, Jiun-Haw Lee, *Senior Member, IEEE*, and Ding-Wei Huang, *Member, IEEE*

***Abstract*—A wavelength division (de)multiplexing (WDM) filter with ultra-low channel crosstalk (XT) and high tolerance was proposed for a 1 × 4 O-band coarse-WDM (CWDM) system on a silicon-on-insulator (SOI). The filter consists of four waveguide Bragg grating (WBG) structures, each one having a multi-mode waveguide and corrugations at both waveguide side walls. To relax the critical dimension, low-material-index silicon nitride (SiN_x) was utilized instead of silicon. For efficient design of each SiN_x multi-mode WBG (MMWBG), the core and corrugation widths were engineered over the perturbed-permittivity coupled-mode theory, leading to an ultra-high side-lobe suppression ratio >25.3 dB. The overall CWDM filter offers flat-top responses with ultra-low excess losses (ELs) <0.6 dB, a high channel uniformity > −0.45 dB, broad 1-dB bandwidths (BWs) ∼13.45 nm, ultra-low XTs <−28 dB, and ultra-broad available bandwidths of 14.35 nm for XTs <−28 dB (ABW_{28-dB} ∼14.35 nm). Analysis of the tolerance showed that XTs of the overall filter remained <−25 dB even for extreme cases with ±18-nm over-etching errors without compromising the ELs or BWs. Given its ultra-low XT, ultra-broad ABW, and high tolerance, the proposed MMWBG shows the great potential and high attractiveness for the O-band CWDM telecommunication systems.**

***Index Terms*—Bragg grating structure, integrated optics, silicon photonics, wavelength division multiplexing system.**

I. Introduction

To MEET the demand for higher processing speed and data capacity brought on by the rapid development of cloud computing, the Internet of Things, and big data, there has been the development of smaller technology nodes, smaller device footprints, and higher integration density chips in accordance with Moore's law [1]. Longer delays, greater loss, and higher crosstalk, however, have been introduced due to the smaller distances of the electrical interconnection of such devices [2]. Some of the resulting issues of the increased densities of interconnection layers, such as electromagnetic interference, bandwidth limitations, increased power consumption, and heat dissipation, have been highlighted in the literature [3], [4], [5], [6], and photonic integrated circuits (PICs) that simultaneously utilize both photonic and electrical devices have been implemented on different platforms to address them [7], [8], [9], [10], [11], [12], [13], [14], [15], [16], [17], [18], [19]. Among these platforms, the silicon-on-insulator (SOI) has gained considerable attention owing to its high level of fabrication maturity.

In the development of SOI utilizing photonic devices, Silicon Photonics (SiPh) has become one of the most important platforms for PICs owing to its superior compatibility with well-developed complementary metal oxide semiconductor technology, enabling mass production at lower cost as well as higher quality [20], [21]. By leveraging these advantages, devices with smaller footprints and lower power requirements can be implemented over SiPh chips. To date, many optical devices [22], [23], [24], [25], [26], [27], [28], [29], [30], [31], [32], [33], [34], [35], [36], [37], [38], [39], [40] have been proposed on the platform to improve telecommunication systems. To further improve performances of some SiPh devices implemented on the SOI platform, a silicon-nitride layer allowing for i) larger band gap, ii) abscence of two-photon or free-carrier absorption in the telecommunication band, iii) ultra-low prapagation loss owing to wide-band transparency window of 0.4–4.5 μm, iv) low nonlinearity in the given transparency window, v) high tolerance to temperature changes [41], [42], and vi) low-index contrast brought by its small material refractive index, has been included and placed above the original silicon layer in the literature [17], [39]. Given that, SiPh foundry services offering silicon-nitride layer over the SOI plaform [39] have emerged and become as another options for PICs using stardard fabrication processes. Among the devices required in the telecommunication systems, the wavelength division (de)multiplexing (WDM) device [18], [19], [31], [32], [33], [34], [35], [43], [44], [45], [46], [47], [48], [49], [50], [51], [52], [53], [54], [55], [56], [57], [58], [59], [60], [61], [62], [63], [64], [65], [66], [67], [68], [69], [70], [71], [72], [73], [74], [75], [76], [77], [78], [79], [80], [81], [82], [83] is one of the most important functions to be used in the

Manuscript received 30 August 2022; revised 20 September 2022; accepted 21 September 2022. Date of publication 26 September 2022; date of current version 30 December 2022. This work was supported by the Ministry of Science and Technology, Taiwan under Grants MOST 110-2224-E-992-001 and MOST 111-2119-M-002-009. *(Corresponding author: Ding-Wei Huang.)*

Kuo-Fang Chung is with the Graduate Institute of Photonics and Optoelectronics, National Taiwan University, Taipei 106319, Taiwan (e-mail: d08941008@ntu.edu.tw).

Tien-Tsorng Shih is with the Department of Electronic Engineering, National Kaohsiung University of Science and Technology, Kaohsiung 807618, Taiwan (e-mail: tt@nkust.edu.tw).

Jiun-Haw Lee and Ding-Wei Huang are with the Graduate Institute of Photonics and Optoelectronics, National Taiwan University, Taipei 106319, Taiwan, and also with the Department of Electrical Engineering, National Taiwan University, Taipei 106319, Taiwan (e-mail: jiunhawlee@ntu.edu.tw; dwhuang@ntu.edu.tw).

Digital Object Identifier 10.1109/JPHOT.2022.3209169

transceiver module of a system, i.e., the transmitter and receiver modules.

To relax misalignments among desired channel, optical lasing, and filtering channel wavelengths due to increased environmental temperature and fabrication errors, some coarse wavelength division (de)multiplexing (CWDM) systems that utilize large channel spacings have been proposed and their capability has already been demonstrated [51], [52], [53], [54], [55], [56], [57], [58], [59], [60], [61], [62], [63], [64], [65], [66], [67], [68], [69], [70], [71], [72], [73], [74], [75], [76], [77], [78], [79]. To broaden the available channel bandwidth (ABW) under the desired low crosstalk (XT) to further improve the communication system, flattened filtering responses are required. In conventional WDM systems that use arrayed waveguide grating (AWG) [80], [81], [82], [83], flattened responses are achieved via the double-image technique; however, this can lead to increased excess losses (ELs) of 2–5 dB [78], [84]. To flatten the filtering responses without compromising ELs, alternative devices based on different mechanisms have been employed [53], [57], [61], [63], [65], [66], [67], [68], [70], [73], [74], [75], [76], [77], [79]. Although low-EL, flat-top, and high-uniformity responses can be obtained using lattice filters based on Mach–Zehnder interferometers (MZIs), the XTs are usually larger than -15 dB because of the narrow splitting/coupling ratio bandwidths at the MZI coupling regions. Bent directional couplers (BDCs) have been used to achieve splitting ratios with broader bandwidths, and XTs below -20 dB have been achieved by leveraging them [74], [75]. However, this was at the expense of the complexity of the coupling patterns.

Another elegant approach to flattening responses is based on the Bragg grating structure (BGS) to achieve low-EL, highly uniform, and flat-top responses [53], [65], [66], [70], [77], [79]. A rectangular response was obtained in [65] with a sinusoidal-profile contra-directional coupling coefficient κ_{ac} by using both amplitude and phase apodizations along the propagation direction. In the literature, the amplitude apodization was achieved using simple tapered waveguides as transitions at the beginning and at the end of a multi-mode waveguide Bragg grating (MMWBG), whereas the phase apodization was obtained by relatively shifting one of the two side-wall BGSs, i.e., width corrugations, along the propagation direction. These led to a sub-decibel EL and low XT below -20 dB owing to the high side-lobe suppression ratios (SLSRs) and near-perfect box-like filtering responses. The silicon-based WBGs, however, were critically dimensioned at 125 nm for the channel wavelength of 1.271 μm by using electron beam lithography. Furthermore, the presented grating periods for four channel wavelengths had drifted from the calculated Bragg periods by $\sim$20 nm due to the non-zero dc-shift term "δ" derived in the perturbed-permittivity CMT [84]; thereby significantly increasing the difficulty of designing such devices and resulting in unbalanced side-lobe suppression at both sides of resonant wavelengths "λ_r", i.e., low side-lobe imbalance (SLI) as defined in Section II. By contrast, XTs can also be further reduced by engineering both amplitude and phase apodizations using Gaussian-like profiles simultaneously. Although this would be at the cost of a slightly higher 20-dB or 25-dB spectral bandwidth (BW_{20-dB} or BW_{25-dB}), such a tradeoff is still acceptable for a CWDM system with a 20-nm channel spacing.

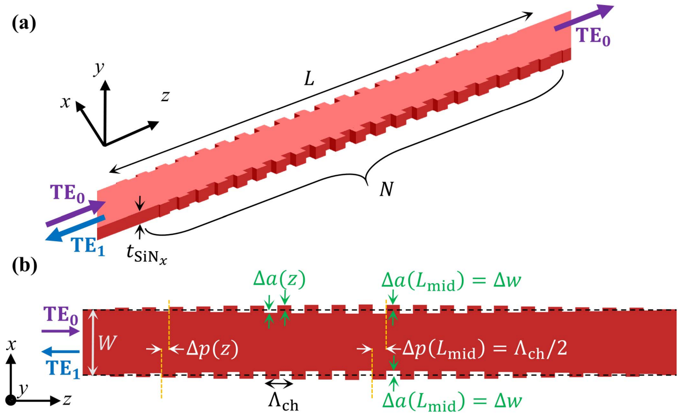

Fig. 1. Schematic **(a)** 3-D and **(b)** top views of the proposed MMWBG.

In this study, a SiN_x-based WDM filter with ultra-low XTs and rectangular responses for an O-band CWDM system on an SOI platform is achieved with MMWBGs using an appropriate core width and properly designed apodizations. In Section II, the working principles of perturbed-permittivity CMT are presented and the MMWBG is proposed with the ultimate aim of relaxing the critical dimension requirements and improving device performance by making acceptable tradeoffs. A suitable waveguide width and its corrugation for amplitude apodization are utilized to simplify the evaluation of resonant wavelengths, allowing for efficient design and balancing of the lobe suppression at both sides of the resonant wavelength. Section III presents an analysis of fabrication error tolerance for future fabrication by a SiPh foundry service, and Section IV presents the conclusions.

II. Device Principle and Optimization

Figure 1 shows the schematic diagrams of the proposed MMWBG that uses a 400-nm-thick silicon-nitride layer for each of the four channels over an SOI platform. The silicon-nitride layer is placed 400 nm above the 220-nm-thick silicon layer of the SOI wafer, to meet the available SiPh foundry service. Each MMWBG is composed of a multi-mode waveguide and corrugations at both side walls of the waveguide such that the forward TE_0 mode can be contra-directionally coupled into the backward TE_1 mode with the filtering response shape of a hyperbolic-tangent function. The reflected TE_1-mode signal is designed to be dropped using a broadband and high-efficiency TE_1–TE_0 asymmetric directional coupler. Circulators for protecting the optical source from reflected signals is not required under this arrangement. To more efficiently determine the required Bragg periods for resonance at the desired channel wavelengths λ_{ch}, perturbed-permittivity CMT principle was utilized. The differential equations of the counter-propagating perturbed-permittivity CMT [84] were minimally adjusted and are given in (1)–(4), where z is the spatial position along the propagation direction, A and B represent the transverse guided-mode amplitudes, and v and μ denote the forward and backward propagation modes, respectively. The parameters ω,

ε_0, and $\varepsilon_{r,(dc,ac)}$ represent the angular frequency determined by the optical wavelength, the permittivity of free space, and the perturbation profile of the relative permittivity constant, respectively. The wavelength-dependent parameters κ, $\Delta\beta$, and ϕ are the coupling coefficient, phase mismatch (detuning), and spatially varying phase change, respectively. The coupling coefficients κ_{dc} and κ_{ac} are obtained by the overlap integration in terms of the dc and ac terms of the permittivity perturbation profile, respectively, and the modes involved in the coupling, whereas $\mathbf{E}$ denotes the normalized transverse electric fields of the guided modes, as given in (3) and (4). The expressions in (5)–(10) describe the contra-directional coupling behavior over a transfer matrix, where α equals $\sqrt{|\kappa_{\rm ac}|^2 - \delta^2}$, and R and S are eigenvalue-dependent representations of the guided-mode amplitudes for the reference (forward) and signal (backward), respectively. The detuning parameter $\Delta\beta$ depends on the guided-mode propagation constants and the harmonic factor decided by the grating period $\lambda_{\rm ch}$ and the harmonic order N, as expressed in (9). In general cases for non-chirped grating structures ($\partial\phi/\partial z = 0$), $N = 1$ and $\Delta\beta = 0$ are employed to determine the required $\lambda_{\rm ch}$ for resonance at desired the channel wavelength $\lambda_{\rm ch}$.

$$\frac{\partial B_\mu}{\partial z} = j\kappa_{\rm dc,\mu\mu} B_\mu + j\kappa_{\rm ac,\nu\mu} A_\nu \cdot e^{-j(\Delta\beta z - \phi(z))}, \tag{1}$$

$$\frac{\partial A_\nu}{\partial z} = -j\kappa_{\rm dc,\nu\nu} A_\nu - j\kappa_{\rm ac,\mu v} B_\mu \cdot e^{j(\Delta\beta z - \phi(z))}, \tag{2}$$

$$\kappa_{\rm dc,(\nu\nu,\mu\mu)} = \frac{\omega\varepsilon_0}{4} \iint \Delta\varepsilon_{\rm r,dc}(x,y)\mathbf{E}_{\nu,\mu}(x,y) \cdot \mathbf{E}^*_{\nu,\mu}(x,y) \times {\rm d}x{\rm d}y, \tag{3}$$

$$\kappa_{\rm ac,(\nu\mu,\mu\nu)} = \frac{\omega\varepsilon_0}{4} \iint \Delta\varepsilon_{\rm r,ac}(x,y)\mathbf{E}_{\nu,\mu}(x,y) \cdot \mathbf{E}^*_{\mu,\nu}(x,y) \times {\rm d}x{\rm d}y, \tag{4}$$

$$\begin{bmatrix} R(z) \\ S(z) \end{bmatrix} = \begin{bmatrix} T_{11}(z) & T_{12}(z) \\ T_{21}(z) & T_{22}(z) \end{bmatrix} \begin{bmatrix} R(0) \\ S(0) \end{bmatrix}, \tag{5}$$

$$T_{11(22)}(z) = \cosh(\alpha z) \underset{(+)}{\overset{-}{}} j\frac{\delta}{\alpha}\sinh(\alpha z), \tag{6}$$

$$T_{12(21)}(z) = \underset{(+)}{\overset{-}{}} j\frac{\kappa_{\rm ac,\{\mu\nu(\nu\mu)\}}}{\alpha}\sinh(\alpha z), \tag{7}$$

$$\delta = \frac{1}{2}(\kappa_{\rm dc,\nu\nu} + \kappa_{\rm dc,\mu\mu} + \Delta\beta), \tag{8}$$

$$\Delta\beta = \beta_\nu + \beta_\mu - \frac{2\pi N}{\Lambda}, \tag{9}$$

$$\left|\frac{S(0)}{R(0)}\right|^2_{S(L)=0} = \left|\frac{-j\frac{\kappa_{\rm ac,\nu\mu}}{\alpha}\sinh(\alpha L)}{\cosh(\alpha L) + j\frac{\delta}{\alpha}\sinh(\alpha L)}\right|^2. \tag{10}$$

The resonant wavelength λ_r, i.e., the wavelength with the maximum reflected signal spectral transmission, can deviate away from the desired channel wavelength $\lambda_{\rm ch}$ due to the non-zero dc-shift term δ, which is the non-zero sum of the two

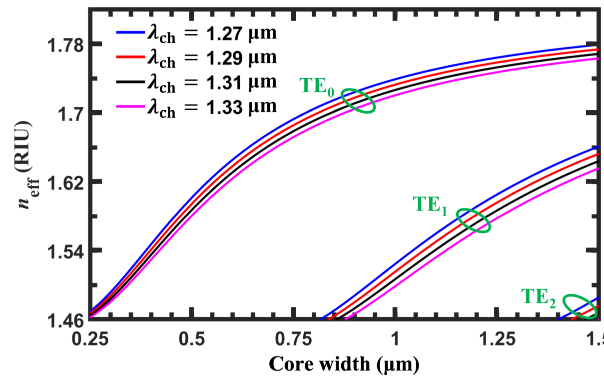

Fig. 2. Effective refractive indices of the first three TE modes versus core widths for four channel wavelengths.

TABLE I
REQUIRED BRAGG PERIODS FOR THE FOUR-CHANNEL CWDM SYSTEM

$\lambda_{\rm ch}$ (μm)	1.27	1.29	1.31	1.33
$\Lambda_{\rm ch}$ (nm)	392	400	408	416

coupling coefficients $\kappa_{\rm dc,\nu\nu}$ and $\kappa_{\rm dc,\mu\mu}$ obtained in (8). Note that an adjustment is made in (8) to cater to the reflected guided $\rm TE_1$ mode denoted by $\kappa_{\rm dc,\mu\mu}$. In (10), the reflected signal at λ_r is obtained by the assumption of no reflected signal amplitude at the end of WBG, i.e., $S(L) = 0$, where L is the full length. From this expression, the maximum transmission of $|\tanh(\alpha(\lambda_{\rm r})L)|^2$ can be achieved with $\delta(\lambda_{\rm r}) = 0$. For efficient design of such device, the condition $\lambda_r = \lambda_{\rm ch}$ should be met so that only the information of guided-mode effective indices and $\lambda_{\rm ch}$ are required to evaluate the Bragg period.

To meet the condition, $\delta(\lambda_{\rm ch}) = 0$, namely $\kappa_{\rm dc,vv} = \kappa_{\rm dc,\mu\mu} = 0$, is engineered with a tailored width for the multi-mode waveguide. A core width of the MMWBG is chosen to achieve approximately identical positive and negative index changes in terms of identical width variation for the $\rm TE_0$ and $\rm TE_1$ modes, respectively. In addition, to guide both the $\rm TE_0$ and $\rm TE_1$ modes and to achieve shorter length of the $\rm TE_1$-mode dropping device, which is presented in following paragraphs, the core width allowing for smaller $\rm TE_1$-mode effective indices with lower confinements at the four channel wavelengths is utilized. A relation between the TE-mode effective indices and the core widths is characterized in Fig. 2 using the finite-difference-eigenmode (FDE) solution (Lumerical Inc.) to determine the appropriate width. Based on the curve shown in Fig. 2, the core width of 950 nm and the corrugated structure for the amplitude apodization shown in Fig. 1(b) are determined to satisfy $\lambda_r = \lambda_{\rm ch}$, and consequently the required Bragg period for resonance can be simply evaluated using the phase matching condition $\Delta\beta = 0$, or an equivalent expression of $\Lambda_{\rm ch} = \lambda_{\rm ch}/(n_{\rm eff}^{\rm TE_1} + n_{\rm eff}^{\rm TE_0})$ as given in Table I.

For an ultra-low XT leveraging the spatial Fourier transform, both amplitude and phase apodizations are applied on the corrugated width to obtain $\kappa_{\rm ac}(z)$ with a sinusoidal profile. The

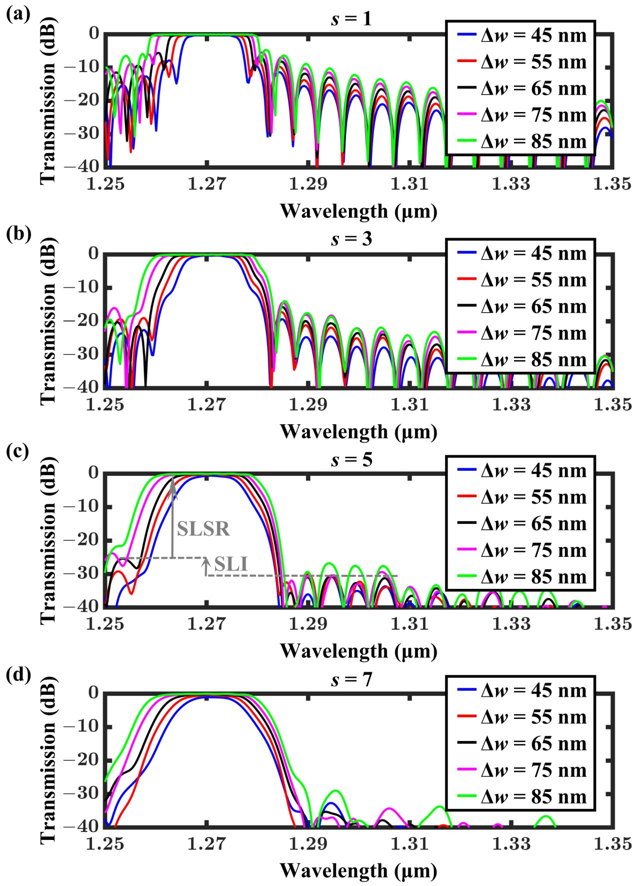

Fig. 3. Simulated filtering responses using 3-D FDTD method for $\lambda_{\text{ch}} = 1.27\ \mu$m in terms of $\Lambda_{\text{ch}} = 392$ nm and different maximum width corrugations Δw.

expressions obtained by

$$\Delta a(z) = \Delta w \cdot \exp\left(-\left(\frac{z - L_{\text{mid}}}{L/\sqrt{s_{\text{a}}}}\right)^2\right) \text{ and} \tag{11}$$

$$\Delta p(z) = \frac{\Lambda_{\text{ch}}}{2} \cdot \exp\left(-\left(\frac{z - L_{\text{mid}}}{L/\sqrt{s_{\text{p}}}}\right)^2\right) \tag{12}$$

illustrate the amplitude apodization $\Delta a(z)$ and phase apodization $\Delta p(z)$, respectively, where $\Delta a(L_{\text{mid}}) = \Delta w$ and $\Delta p(L_{\text{mid}}) = \Lambda_{\text{ch}}/2$ are used to achieve the maximum value of κ_{ac} at half of the full length, i.e., $z = L_{\text{mid}} = L/2$. For simplification, the apodization strengths s_{a} and s_{p} in (11) and (12), respectively, are assigned the same value s under a fixed duty cycle of 0.5. Figure 3 depicts the simulated filtering responses using the three-dimensional (3-D) finite-difference time-domain (FDTD) method (Lumerical Inc.). The calculated period of 392 nm (Table I) is utilized in a 3-D model for resonance at the channel wavelength λ_{ch} of 1.27 μm. Both apodizations are employed at different Δw ranging from 45 to 85 nm in a step of 10 nm and s ranging from 1 to 7 in a step of 2. For a flat-top response with a 1-dB channel BW ($\text{BW}_{\text{1-dB}}$) of 14 nm and SLI as defined in Fig. 3(c) that remains below 5 dB while the SLSR remains above 25.5 dB, the parameter set

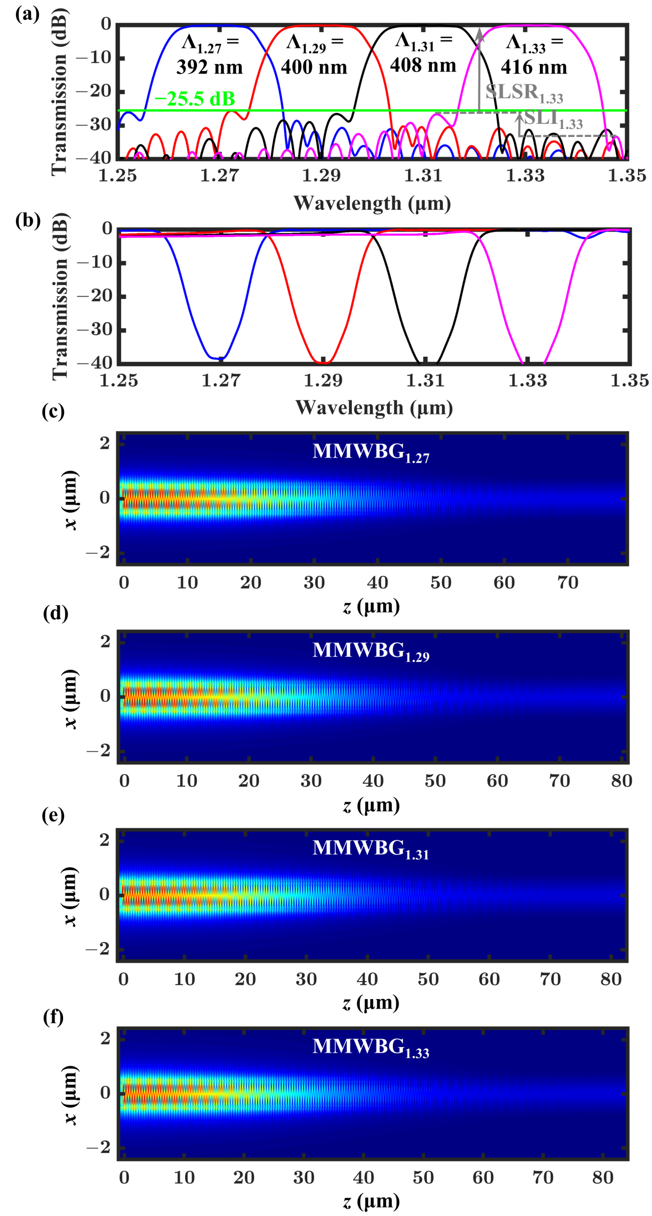

Fig. 4. Simulated filtering responses of **(a)** the contra-directional coupled TE_1 mode, **(b)** the remaining forward TE_0 mode, and **(c)–(f)** the electric-field top-view profiles at the given four channel wavelengths, respectively, for the corresponding individual MMWBGs using the 3-D FDTD solutions in terms of the parameter set (W, Δw, s) = (950 nm, 65 nm, 5).

(Δw, s) of (65 nm, 5) is utilized in the following simulations. The filtering responses of the four individual MMWBGs, which are critically dimensioned at 196 nm and achievable at a representative SiPh foundry, given in Fig. 4 show that ultra-low ELs below 0.3 dB, high uniformity above −0.035 dB, and ultra-low XTs below −25.5 dB are achieved. The ultra-low XTs are attributed to the high SLSRs above 25.5 dB, and the low SLIs of approximately 2.5, 4.63, 6, and 6.66 dB for Channels 1.27, 1.29, 1.31, and 1.33 μm, respectively. Moreover, the available bandwidth for XTs below −25 dB ($\text{ABW}_{\text{25-dB}}$) reaches 13.5 nm, which is beneficial for performances of the overall CWDM filter.

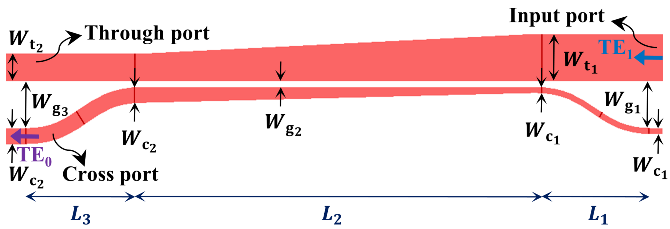

Fig. 5. Schematic top view of the SiN_x-based BADC for broadband coupling from the TE_1 mode at through port to the TE_0 mode at cross port.

TABLE II
OPTIMAL PARAMETER SET OF SiN_x-BASED BADC

Parameter	W_{t_1}	W_{t_2}	W_{c_1}	W_{c_2}
Value (µm)	1.305	0.86	0.15	0.395
Parameter	W_{g_1}	W_{g_2}	W_{g_3}	
Value (µm)	1.145	0.23	0.36	
Parameter	L_1	L_2	L_3	
Value (µm)	29.335	80.785	34.94	

To drop the reflected TE_1-mode signal using four identical devices at the corresponding channels, a broadband asymmetrical directional coupler (BADC) based on silicon nitride over the SOI platform is designed at the entrance of each MMWBG. Under this arrangement, its fabrication tolerance analysis is not necessary given that broadband devices usually allows for low sensitivity to geometry, if the devices are sufficiently large. In addition, the mesh accuracy required for the BADC simulation can be significantly reduced owing to the broadband performance as well as the lower sensitivity to geometry, greatly saving the demanded optimization time using a user-defined algorithm. Figure 5 shows the schematic top view of the BADC, with the input/through and cross ports carrying the counter-propagating TE_1 and TE_0 modes, respectively. The design methodology proposed in [36] is utilized for an optimization using the 3-D FDTD method in combination with a user-defined adaptive particle swarm algorithm APSO [85] to obtain high coupling efficiencies in the given wavelength span. To guide at the two lowest modes obtained in Fig. 3 and to achieve an adiabatic coupling at the region within the length denoted by L_1, W_{t_2} and W_{c_1} is fixed at the core width 860 nm and the critical dimension 150 nm, respectively, while the remaining parameters given in Fig. 5 optimized using the user-defined APSO. Table II lists the optimal parameter set to achieve a broadband coupling response from the TE_1 mode at the input/through port to the TE_0 mode at the cross port. The simulated transmission and spectral response of the extinction ratio (ER) between the TE_0 and TE_1 modes are respectively depicted in Fig. 6(a) with blue and red curves, where the ER is defined as

$$\mathrm{ER} = 10 \cdot \log_{10}\left(T_{\mathrm{TE}_0}^{\mathrm{cross}} / T_{\mathrm{TE}_1}^{\mathrm{through}}\right), \qquad (13)$$

with electric-field profiles at corresponding wavelengths given in Fig. 6(b)–(g). From the results, the TE_1–TE_0 coupling ratios above 98.63 % (> -0.06 dB) and ultra-high ERs above 40 dB are achieved within the wavelength span of 1.25–1.35 μm, demonstrating the feasibility of dropping the TE_1 mode efficiently without compromising the filtering responses of the MMWBGs. Note that a high fabrication tolerance of the BADC can be reasonably assumed so that only the tolerance of the MMWBGs are analyzed in the following section, owing to i) the low-index contrast in terms of the core (silicon nitride) and cladding (silicon dioxide) materials, ii) the ultra-high and broadband coupling efficiency, and iii) the large footprint of the BADC. To evaluate the performances of the overall O-band CWDM filter, four groups for the corresponding channels are cascaded in a proper order, with each group formed by the same BADC followed by the MMWBG designed for the desired channel. Regarding the cascading order, the MMWBG desgined for the shorter channel wavelength is cascaded with higher priority to conduct the contra-directional coupling when demultiplexing, given that the MMWBGs designed for longer channel wavelengths would compromise the forward TE_0-mode transmission at shorter wavelengths by approximately 1–2 dB, as shown in Fig. 4(b). Fig. 7 illustrates the schematic configuration of the overall O-band CWDM filter as well as its simulated filtering responses. The simulation results show that the flat-top responses with low ELs below 1 dB (0.17/0.3/0.4/0.6 dB at 1.27/1.29/1.31/1.33 μm), a high channels uniformity above -0.45 dB, a broad $BW_{1\text{-dB}}$ $\sim$13.45 nm, an ultra-low channel XT of -28 dB, ultra-broad $ABW_{28\text{-dB}}$ and $ABW_{20\text{-dB}}$ of approximately 14.35 and 15.7 nm, respectively, are obtained. Table III shows performance comparison, indicating the ultra-low channel XT of -28 dB with its ultra-broad available bandwidth $\sim$14.35 nm, outperforming all other CWDM filters in the literature.

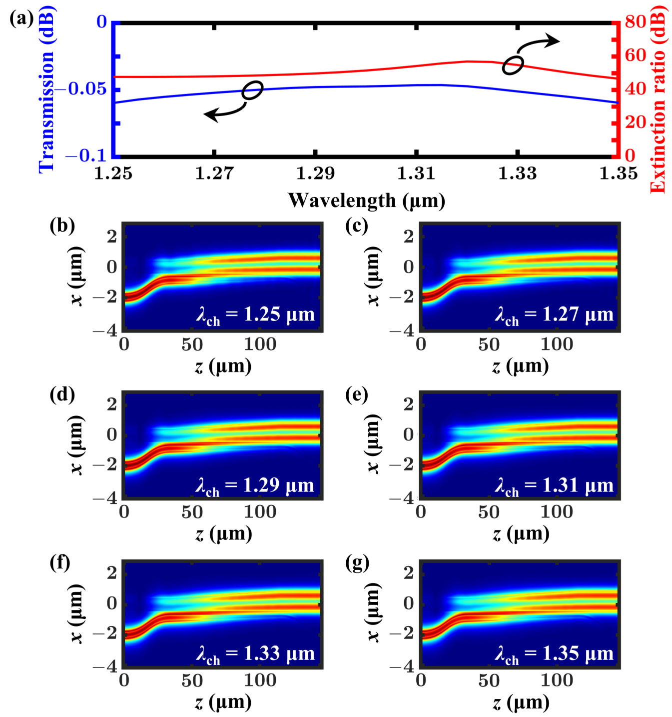

Fig. 6. **(a)** Simulated transmission (blue) of the TE_0 mode at cross port, and extinction ratio (red) between the dropped TE_0 and remaining TE_1 modes. **(b)–(g)** Electric-field profiles at six wavelengths.

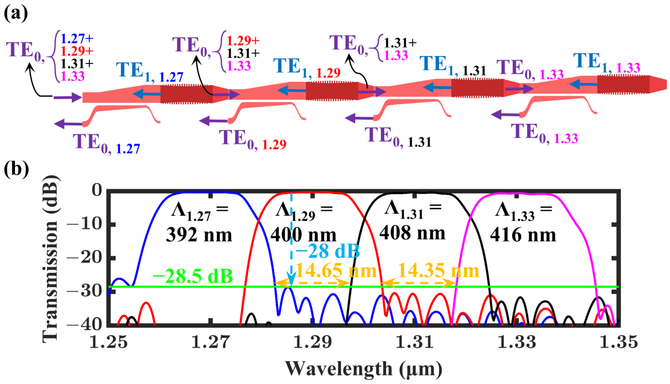

Fig. 7. **(a)** Schematic configuration of the proposed overall O-band CWDM filter and **(b)** its simulated filtering responses.

TABLE III
PERFORMANCE COMPARISON OF CWDM FILTERS IN THE LITERATURE

Structure	EL (dB)	XT (dB)	Mat./ Band	$BW^{a}_{1\text{-dB}}$ (nm)	$ABW^{b}_{20\text{-dB}}$ (nm)	$ABW^{c}_{28\text{-dB}}$ (nm)
AWG [69] (Fig. 6(a))	5–6	−27	InP/ O	3	< 3	–
AWG [78] (Fig. 14)	∼3	−25	Si/ O	∼11	∼12.8	–
EG[d] [86] (Fig. 5(d))	∼3	−22	Si/ C	∼5.7	∼7.5	–
EG [71] (Fig. 3(c))	2–3	−30	SiN/ O	∼6.7	5.7	< 3
MMI[e] [60] (Fig. 3(d))	2–3	−13	Si/ C	8.5	–	–
MMI [52] (Fig. 6(b))	< 1	−18	LN/ O	7.5	–	–
MZI [61] (FIg. 6(b))	∼0.5	−16	Si/ C	∼14	–	–
MZI [75] (Fig. 5(d))	< 1	−23	Si/ O	18	∼3.7	–
MZI [57] (Fig. 3(b))	1.78	−15	SiN/ O	11.86	–	–
WBG[f] [70] (Fig. 6(b))	∼1	−12	Si/ C	12	–	–
WBG [53] (Fig. 7)	< 1	−13	Si/ C	7	–	–
WBG [65] (Fig. 5(c))	∼1	−20	Si/ O	15	∼12	–
WBG [66] (Fig. 5(b))	< 1.1	−18	LN/ C	10	–	–
Proposed Structure	< 1	**−28**	SiN/ O	**13.45**	**∼15.7**	**14.35**

[a] 1-dB bandwidth measured from the transmission peak.
[b] Available bandwidth for channel XT below −20 dB, *i.e.*, $ABW_{20\text{-dB}}$.
[c] Available bandwidth for channel XT below −28 dB, *i.e.*, $ABW_{28\text{-dB}}$.
[d] Echelle grating; [e] Multi-mode interferometer; [f] Waveguide Bragg grating.

III. Analysis of Fabrication Tolerance

As mentioned earlier in the former section, only the tolerance of the proposed MMWBG to fabrication errors is analyzed to evaluate the overall device robustness, under the reasonable assumption of the high tolerance for the BADC. To ensure that a sufficient degree of robustness would be demonstrated, a value that is three times the standard error during manufacture is selected for the analysis. Given a standard error of 6 nm provided by a representative foundry service, an over-etching error W_e within ±18 nm with a step of 6 nm is used to evaluate the

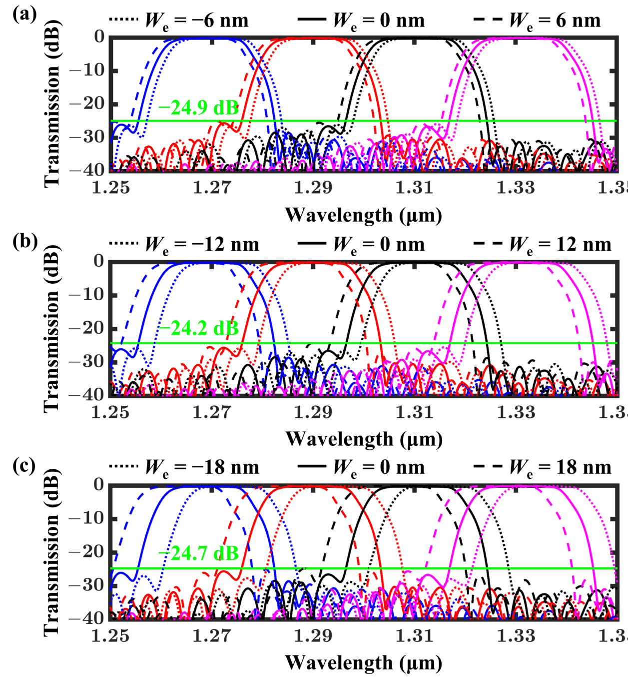

Fig. 8. Simulated filtering responses of the individual MMWBGs using 3-D FDTD method at the four channels in terms of the configuration in Fig. 1 and the given over-etching errors W_e within (±18 nm) with a step of 6 nm.

tolerance. For each tolerance analysis, the patterned core region is considered as an island, with the outermost region (width and length) decreased/increased by the fabrication error. The concept is utilized so that both the corrugated width and duty cycle of the WBG are adjusted in terms of W_e. Figure 8 shows the filtering responses of the proposed MMWBGs at four channels in terms of the different over-etching errors. The corresponding resonant wavelengths is as expected, appearing blue-shifted (red-shifted) due to the decreased (increased) effective indices of both the TE_0 and TE_1 modes owing to the over-etching errors $W_e > 0$ ($W_e < 0$). The XTs given in Fig. 8 remain below −24.2 dB even in the case of three times the standard error, i.e., ±18 nm, demonstrating the high tolerance to fabrication error of the proposed device for the O-band CWDM system. The resulting high fabrication tolerance can be attributed to three advantageous conditions: i) low index contrast brought by the utilized silicon-nitride layer, ii) a wide core width allowing for guiding the TE_1 mode but at the small effective indices at four channels, iii) the coarse channel spacing of 20 nm configured for the CWDM systems. To ensure the filter is entirely considered, simulated filtering responses of the overall CWDM filter at the different over-etching errors W_e are conducted using the compact model based on the S-parameter concept, as shown in Fig. 9. The simulation results indicate the impact of the deviated MMWBGs on the performances of the overall CWDM filter, illustrating the flat-top responses offering a low EL below 1 dB and an ultra-low XT below −25 dB even for the extreme cases with $W_e = \pm 18$ nm, showing the great potential and high attractiveness of the device for use in the O-band CWDM systems.

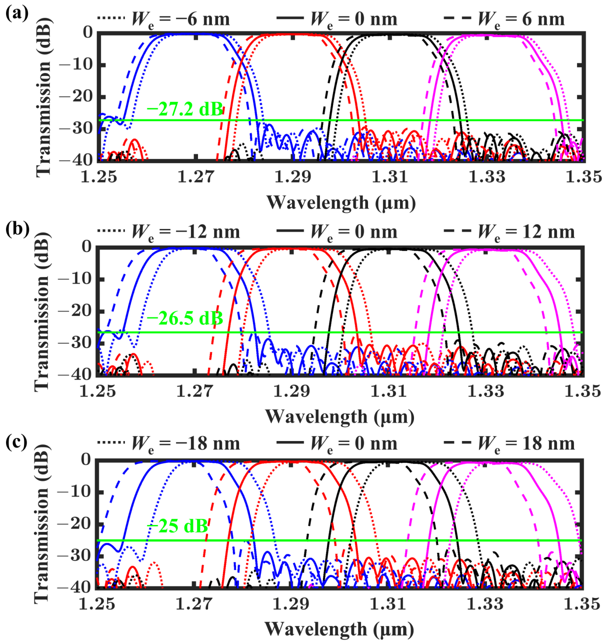

Fig. 9. Simulated filtering responses of the overall CWDM filter using 3-D FDTD method followed by cascaded S-parameter calculation at the four channels in terms of the configuration in Fig. 7 and the given over-etching errors W_{e}.

IV. Conclusion

A wavelength division (de)multiplexing (WDM) filter with ultra-low channel crosstalk (XT) and high fabrication tolerance was achieved using multi-mode waveguide Bragg grating (MMWBG). The device was based on a silicon-nitride layer over a silicon-on-insulator to achieve the critical dimension of ≥ 150 nm to permit future fabrication at a SiPh foundry service. By introducing an appropriate and balanced width corrugation, i.e., the same positive and negative width change referenced to the unperturbed width, into the amplitude apodization, the dc-shift term of the permittivity perturbation was eliminated to allow for efficient design of the required Bragg period, so that the period can be evaluated by simply using channel wavelengths and guided-mode effective indices. For lower XTs, phase apodization was also employed to achieve a sinusoidal profile of the coupling ac term. The results indicated that an ultra-low channel XT below −28 dB, an ultra-broad available bandwidth of 14.35 nm for channel XT below −28 dB ($\mathrm{ABW}_{28\text{-dB}}$ ∼14.35 nm), an ultra-broad $\mathrm{ABW}_{20\text{-dB}}$ ∼15.7 nm, and a high tolerance to fabricated errors within (±18 nm) were achieved, showing the great potential and high attractiveness of the proposed MMWBGs for use in the O-band CWDM telecommunication systems.

Acknowledgment

The authors would like to thank Taiwan Semiconductor Research Institute (TSRI), especially Zheng-Shun Liu, Dr. Hua-Kung Chiu, and Dr. Ming-Wei Lin, for the kindly help with the device fabrication for future tape out.

References

[1] L. Wilson, "International technology roadmap for semiconductors (ITRS)," *Semicond. Ind. Assoc.*, vol. 1, Aug. 2013. Accessed: Aug. 2022. [Online]. Available: https://www.semiconductors.org/resources/2013-international-technology-roadmap-for-semiconductors-itrs/

[2] B. Doyle et al., "Transistor elements for 30nm physical gate lengths and beyond," *Intel Technol. J.*, vol. 6, no. 2, pp. 42–54, May 2002. Accessed: Aug. 2022. [Online]. Available: https://citeseerx.ist.psu.edu/viewdoc/summary?doi=10.1.1.14.9956

[3] J. A. Davis et al., "Interconnect limits on gigascale integration (GSI) in the 21st century," *Proc. IEEE*, vol. 89, no. 3, pp. 305–324, Mar. 2001, doi: 10.1109/5.915376.

[4] L. Benini and G. D. Micheli, "Networks on chips: A new SoC paradigm," *Computer*, vol. 35, no. 1, pp. 70–78, Jan. 2002, doi: 10.1109/2.976921.

[5] J. Henkel et al., "On-chip networks: A scalable, communication-centric embedded system design paradigm," in *Proc. 17th Int. Conf. VLSI Des.*, 2004, pp. 845–851, doi: 10.1109/ICVD.2004.1261037.

[6] A. Gerstlauer et al., "Automatic network generation for system-on-chip communication design," in *Proc. 3rd IEEE/ACM/IFIP Int. Conf. Hardware/Softw. Codesign System Synth.*, 2005, pp. 255–260, doi: 10.1145/1084834.1084899.

[7] M. J. R. Heck et al., "Hybrid silicon photonic integrated circuit technology," *IEEE J. Sel. Topics Quantum Electron.*, vol. 19, no. 4, pp. 6100117–6100117, Jul./Aug. 2013, doi: 10.1109/JSTQE.2012.2235413.

[8] R. Nagarajan et al., "Large-scale photonic integrated circuits," *IEEE J. Sel. Topics Quantum Electron.*, vol. 11, no. 1, pp. 50–65, Jan./Feb. 2005, doi: 10.1109/JSTQE.2004.841721.

[9] T. L. Koch and U. Koren, "Semiconductor photonic integrated circuits," *IEEE J. Quantum Electron.*, vol. 27, no. 3, pp. 641–653, Mar. 1991, doi: 10.1109/3.81373.

[10] M. J. Wale, "InP PIC design and manufacture: A. new way forward," in *Proc. ICO Int. Conf. Inf. Photon.*, 2011, pp. 1–2, doi: 10.1109/ICO-IP.2011.5953798.

[11] J. T. Kim and S.-Y. Choi, "Graphene-based plasmonic waveguides for photonic integrated circuits," *Opt. Exp.*, vol. 19, no. 24, pp. 24557–24562, Nov. 2011, doi: 10.1364/OE.19.024557.

[12] J. T. Kim et al., "Graphene-based plasmonic photodetector for photonic integrated circuits," *Opt. Exp.*, vol. 22, no. 1, pp. 803–808, Jan. 2014, doi: 10.1364/OE.22.000803.

[13] N. Nozhat and N. Granpayeh, "Analysis of the plasmonic power splitter and MUX/DEMUX suitable for photonic integrated circuits," *Opt. Commun.*, vol. 284, no. 13, pp. 3449–3455, Jun. 2011, doi: 10.1016/j.optcom.2011.03.007.

[14] S. Mohammadi-Pouyan et al., "High-performance Mach-Zehnder modulator using tailored plasma dispersion effects in an ITO/graphene-based waveguide," *Sci. Rep.*, vol. 12, no. 1, p. 12738, Jul. 2022, doi: 10.1038/s41598-022-17125-y.

[15] Q. Wilmart et al., "A hybrid SOI/SIN photonic platform for high-speed and temperature-insensitive cwdm optical transceivers," in *Proc. SPIE*, 2018, Art. no. 1053709, doi: 10.1117/12.2289633.

[16] L. Chrostowski et al., "Silicon photonic resonator sensors and devices," *Proc. SPIE*, vol. 8236, Feb. 2012, Art. no. 823620, doi: 10.1117/12.916860.

[17] D. J. Blumenthal et al., "Silicon nitride in silicon photonics," *Proc. IEEE*, vol. 106, no. 12, pp. 2209–2231, Dec. 2018, doi: 10.1109/JPROC.2018.2861576.

[18] A. Malik et al., "Germanium-on-silicon mid-infrared arrayed waveguide grating multiplexers," *IEEE Photon. Technol. Lett.*, vol. 25, no. 18, pp. 1805–1808, Sep. 2013, doi: 10.1109/LPT.2013.2276479.

[19] D. Martens et al., "Compact silicon nitride arrayed waveguide gratings for very near-infrared wavelengths," *IEEE Photon. Technol. Lett.*, vol. 27, no. 2, pp. 137–140, Jan. 2015, doi: 10.1109/LPT.2014.2363298.

[20] T. Baehr-Jones et al., "Myths and rumours of silicon photonics," *Nature Photon.*, vol. 6, no. 4, pp. 206–208, Mar. 2012, doi: 10.1038/nphoton.2012.66.

[21] M. Hochberg and T. Baehr-Jones, "Towards fabless silicon photonics," *Nature Photon.*, vol. 4, no. 8, pp. 492–494, Aug. 2010, doi: 10.1038/nphoton.2010.172.

[22] Y. C. Tu et al., "High-efficiency ultra-broadband multi-tip edge couplers for integration of distributed feedback laser with silicon-on-insulator waveguide," *IEEE Photon. J.*, vol. 11, no. 4, Aug. 2019, Art. no. 6602113, doi: 10.1109/JPHOT.2019.2924477.

[23] W. Liu et al., "High efficiency silicon edge coupler based on uniform arrayed waveguides with un-patterned cladding," *IEEE Photon. Technol. Lett*., vol. 32, no. 17, pp. 1077–1080, Sep. 2020, doi: 10.1109/lpt.2020.3011188.

[24] J. C. C. Mak et al., "Multi-layer silicon nitride-on-silicon polarization-independent grating couplers," *Opt. Exp*., vol. 26, no. 23, Nov. 2018, Art. no. 30623, doi: 10.1364/oe.26.030623.

[25] B. Chen et al., "Two-dimensional grating coupler on silicon with a high coupling efficiency and a low polarization-dependent loss," *Opt. Exp*., vol. 28, no. 3, pp. 4001–4009, Feb. 2020, doi: 10.1364/OE.380338.

[26] P. Fu et al., "Optimization for ultrabroadband polarization beam splitters using a genetic algorithm," *IEEE Photon. J*., vol. 11, no. 1, Feb. 2019, Art. no. 6600611, doi: 10.1109/JPHOT.2018.2887096.

[27] P.-H. Fu et al., "Broadband optical waveguide couplers with arbitrary coupling ratios designed using a genetic algorithm," *Opt. Exp*., vol. 24, no. 26, pp. 30547–30561, Dec. 2016, doi: 10.1364/OE.24.030547.

[28] C. Ye and D. Dai, "Ultra-compact broadband 2 $\times$ 23 db power splitter using a subwavelength-grating-assisted asymmetric directional coupler," *J. Lightw. Technol*., vol. 38, no. 8, pp. 2370–2375, Apr. 2020, doi: 10.1109/jlt.2020.2973663.

[29] M. Ma et al., "Sub-wavelength grating-assisted polarization splitter-rotators for silicon-on-insulator platforms," *Opt. Exp*., vol. 27, no. 13, pp. 17581–17591, Jun. 2019, doi: 10.1364/OE.27.017581.

[30] W. Lee et al., "Coherent terahertz wireless communication using dual-parallel MZM-based silicon photonic integrated circuits," *Opt. Exp*., vol. 30, no. 2, pp. 2547–2563, Jan. 2022, doi: 10.1364/OE.446516.

[31] S. Pathak et al., "Compact SOI-based polarization diversity wavelength de-multiplexer circuit using two symmetric AWGs," *Opt. Exp*., vol. 20, no. 26, pp. B493–B500, Dec. 2012, doi: 10.1364/OE.20.00B493.

[32] S. Pathak et al., "Effect of mask discretization on performance of silicon arrayed waveguide gratings," *IEEE Photon. Technol. Lett*., vol. 26, no. 7, pp. 718–721, Apr. 2014, doi: 10.1109/LPT.2014.2303793.

[33] J. Zou et al., "Novel wavelength multiplexer using (N 1) $\times$ (N 1) arrayed waveguide grating and polarization-combiner-rotator on SOI platform," *J. Lightw. Technol*., vol. 39, no. 8, pp. 2431–2437, Apr. 2021.

[34] S. Pathak et al., "Design trade-offs for silicon-on-insulator-based AWGs for (de)multiplexer applications," *Opt. Lett*., vol. 38, no. 16, pp. 2961–2964, Aug. 2013, doi: 10.1364/OL.38.002961.

[35] D. Melati et al., "Compact and low crosstalk echelle grating demultiplexer on silicon-on-insulator technology," *Electronics*, vol. 8, no. 6, Jun. 2019, Art. no. 687, doi: 10.3390/electronics8060687.

[36] D. Dai et al., "10-channel mode (de)multiplexer with dual polarizations," *Laser Photon. Rev*, vol. 12, no. 1, Jan. 2018, Art. no. 1700109, doi: 10.1002/lpor.201700109.

[37] Z. Wang et al., "Compact silicon three-mode multiplexer by refractive-index manipulation on a multi-mode interferometer," *Opt. Exp*., vol. 29, no. 9, pp. 13899–13907, Apr. 2021, doi: 10.1364/OE.423973.

[38] J. Y. Su et al., "Ge p-i-n photodiode as 60-Gbit/s optical NRZ-OOK data receiver," *J. Lightw. Technol*., vol. 40, no. 13, pp. 4326–4336, Jul. 2022, doi: 10.1109/JLT.2022.3161011.

[39] X. Hu et al., "High-speed and high-power germanium photodetector with a lateral silicon nitride waveguide," *Photon. Res*., vol. 9, no. 5, pp. 749–756, May 2021, doi: 10.1364/PRJ.417601.

[40] Y. Li and R. Baets, "Improved multi-mode interferometers (MMIs) on silicon-on-insulator with the optimized return loss and isolation," in *Proc. 16th Annu. Symp. IEEE Photononics Benelux Chapter*, Dec. 2011, pp. 205–208.

[41] M. Piels et al., "Low-loss silicon nitride awg demultiplexer heterogeneously integrated with hybrid III–V/silicon photodetectors," *J. Lightw. Technol*., vol. 32, no. 4, pp. 817–823, Feb. 2014.

[42] D. Dai et al., "Low-loss Si_3N_4 arrayed-waveguide grating (de)multiplexer using nano-core optical waveguides," *Opt. Exp.*, vol. 19, no. 15, pp. 14130–14136, Jul. 2011, doi: 10.1364/OE.19.014130. [Online]. Available: http://opg.optica.org/oe/abstract.cfm?URI=oe- 19-15-14130

[43] T. D. Bucio et al., "Silicon nitride photonics for the near-infrared," *IEEE J. Sel. Topics Quantum Electron*., vol. 26, no. 2, pp. 1–13, Mar.–Apr. 2020, doi: 10.1109/jstqe.2019.2934127.

[44] D. Daoxin et al., "Multimode silicon photonic devices," in *Proc. SPIE*, 2021, vol. 11689, doi: 10.1117/12.2577026.

[45] D. Daoxin et al., "Silicon photonic devices for wavelength/mode-division-multiplexing," in *Proc. SPIE*, 2021, vol. 11775, pp. 28–39, doi: 10.1117/12.2588925.

[46] N. Saha et al., "Tunable narrow band add-drop filter design based on apodized long period waveguide grating assisted co-directional coupler," *Opt. Exp*., vol. 30, no. 16, pp. 28632–28646, Aug. 2022, doi: 10.1364/OE.461876.

[47] J. Jiang et al., "Silicon lateral-apodized add–drop filter for on-chip optical interconnection," *Appl. Opt*., vol. 56, no. 30, pp. 8425–8429, Oct. 2017, doi: 10.1364/AO.56.008425.

[48] L. Liu et al., "Dual functional WDM devices for multiplexing and demultiplexing on silicon-on-insulator," in *Proc. Int. Photon. Optoelectron. Meeting*, 2017, pp. AS3A–25, doi: 10.1364/ASA.2017.AS3A.25.

[49] S. Kumar et al., "Side-lobe reduction by cascading Bragg grating filters on a Si-photonic chip," *Opt. Exp*., vol. 30, no. 6, pp. 9983–9991, Mar. 2022, doi: 10.1364/OE.446588.

[50] J. Zou et al., "High resolution and ultra-compact on-chip spectrometer using bidirectional edge-input arrayed waveguide grating," *J. Lightw. Technol*., vol. 38, no. 16, pp. 4447–4453, Aug. 2020.

[51] T. D. Bucio et al., "N-rich silicon nitride angled mmi for coarse wavelength division (de)multiplexing in the o-band," *Opt. Lett*., vol. 43, no. 6, Mar. 2018, Art. no. 1251, doi: 10.1364/ol.43.001251.

[52] G. Chen et al., "Four-channel CWDM device on a thin-film lithium niobate platform using an angled multimode interferometer structure," *Photon. Res*., vol. 10, no. 1, pp. 8–13, Jan. 2022, doi: 10.1364/prj.438816.

[53] J. Chen and Y. Shi, "Flat-top CWDM (de)multiplexers based on contra-directional couplers with subwavelength gratings," *IEEE Photon. Technol. Lett*., vol. 31, no. 24, pp. 2003–2006, Nov. 2019, doi: 10.1109/LPT.2019.2953379.

[54] S. Cheung and M. R. Tan, "Ultra-low loss and fabrication tolerant silicon nitride (Si_3N_4) (de-)muxes for 1-μm cwdm optical interconnects," in *Proc. Opt. Fiber Commun. Conf.*, 2020, pp. M3F–6, doi: 10.1364/OFC.2020.M3F.6.

[55] S. S. Cheung and M. R. T. Tan, "Silicon nitride (Si_3N_4) (de-)multiplexers for 1-μm CWDM optical interconnects," *J. Lightw. Technol*., vol. 38, no. 13, pp. 3404–3413, Nov. 2020, doi: 10.1364/JLT.38.003404.

[56] C. R. Doerr et al., "Eight-channel SiO_2/Si_3N_4/Si/Ge CWDM receiver," *IEEE Photon. Technol. Lett*., vol. 23, no. 17, pp. 1201–1203, Sep. 2011, doi: 10.1109/LPT.2011.2158091.

[57] G. Gao et al., "Silicon nitride O-band (de)multiplexers with low thermal sensitivity," *Opt. Exp*., vol. 25, no. 11, May 2017, Art. no. 12260, doi: 10.1364/oe.25.012260.

[58] S. Guerber et al., "Polarization independent and temperature tolerant AWG based on a silicon nitride platform," *Opt. Lett*., vol. 45, no. 23, Dec. 2020, Art. no. 6559, doi: 10.1364/ol.411332.

[59] S. Guerber et al., "Design and integration of an O-band silicon nitride AWG for CWDM applications," in *Proc. IEEE 14th Int. Conf. Group IV Photon.*, Aug. 2017, pp. 133–134, doi: 10.1109/GROUP4.2017.8082232.

[60] Y. Hu et al., "Wavelength division (de)multiplexing based on dispersive self-imaging," *Opt. Lett*., vol. 36, no. 23, pp. 4488–4490, Dec. 2011, doi: 10.1364/OL.36.004488.

[61] X. Jiang et al., "Compact CWDM interleaver based on an interfering loop containing a one-dimensional Fabry-Perot cavity," *Opt. Lett*., vol. 43, no. 5, pp. 1071–1074, Mar. 2018, doi: 10.1364/OL.43.001071.

[62] S. Kim and M. Qi, "Post-fabrication trimming on silicon nitride photonic bragg grating add-drop filter," in *Proc. Front. Opt.*, 2014, pp. FTu4D–5, doi: 10.1364/FIO.2014.FTu4D.5.

[63] J. Y. Lee et al., "Fabrication-tolerant nitride lattice filter for cwdm," in *Proc. Opt. Fiber Commun. Conf.*, 2021, pp. Tu5B–2, doi: 10.1364/OFC.2021.Tu5B.2.

[64] D. Liu et al., "Silicon photonic filters," *Microw. and Opt. Technol. Lett*., vol. 63, no. 9, pp. 2252–2268, Jul. 2020, doi: 10.1002/mop.32509.

[65] D. Liu et al., "Four-channel CWDM (de)multiplexers using cascaded multimode waveguide gratings," *IEEE Photon. Technol. Lett*., vol. 32, no. 4, pp. 192–195, Feb. 2020, doi: 10.1109/LPT.2020.2966073.

[66] Y. Liu et al., "C-band four-channel CWDM (de-)multiplexers on a thin film lithium niobate–silicon rich nitride hybrid platform," *Opt. Lett*., vol. 46, no. 19, pp. 4726–4729, Oct. 2021, doi: 10.1364/OL.437681.

[67] J. C. Mikkelsen et al., "Polarization-insensitive silicon nitride Mach-Zehnder lattice wavelength demultiplexers for CWDM in the o-band," *Opt. Exp*., vol. 26, no. 23, Nov. 2018, Art. no. 30076, doi: 10.1364/oe.26.030076.

[68] J. R. Ong et al., "Wafer-level characterization of silicon nitride CWDM (de)multiplexers using Bayesian inference," *IEEE Photon. Technol. Lett*., vol. 32, no. 15, pp. 917–920, Aug. 2020, doi: 10.1109/LPT.2020.3004850.

[69] P. Pan et al., "Compact 4-channel AWGs for CWDM and LAN WDM in data center monolithic applications," *Opt. Laser Technol.*, vol. 75, pp. 177–181, Dec. 2015, doi: 10.1016/j.optlastec.2015.07.005.
[70] W. Shi et al., "Ultra-compact, flat-top demultiplexer using anti-reflection contra-directional couplers for CWDM networks on silicon," *Opt. Exp.*, vol. 21, no. 6, pp. 6733–6738, Mar. 2013, doi: 10.1364/OE.21.006733.
[71] Q. Wilmart et al., "A versatile silicon-silicon nitride photonics platform for enhanced functionalities and applications," *Appl. Sci.*, vol. 9, no. 2, Jan. 2019, Art. no. 255, doi: 10.3390/app9020255.
[72] Q. Wilmart et al., "Si-sin photonic platform for cwdm applications," in *Proc. IEEE 15th Int. Conf. Group IV Photon.*, 2018, pp. 1–2, doi: 10.1109/GROUP4.2018.8478747.
[73] H. Xu et al., "Low-crosstalk and fabrication-tolerant four-channel CWDM filter based on dispersion-engineered Mach-Zehnder interferometers," *Opt. Exp.*, vol. 29, no. 13, p. 20617, Jun. 2021, doi: 10.1364/oe.428352.
[74] H. Xu et al., "Polarization-insensitive four-channel coarse wavelength-division (de)multiplexer based on Mach-Zehnder interferometers with bent directional couplers and polarization rotators," *Opt. Lett.*, vol. 43, no. 7, pp. 1483–1486, Apr. 2018, doi: 10.1364/OL.43.001483.
[75] H. Xu and Y. Shi, "Flat-top CWDM (de)multiplexer based on MZI with bent directional couplers," *IEEE Photon. Technol. Lett.*, vol. 30, no. 2, pp. 169–172, Jan. 2018, doi: 10.1109/LPT.2017.2779489.
[76] T. H. Yen and Y. J. Hung, "Fabrication-tolerant CWDM (de)multiplexer based on cascaded Mach-Zehnder interferometers on silicon-on-insulator," *J. Lightw. Technol.*, vol. 39, no. 1, pp. 146–153, Jan. 2021, doi: 10.1109/JLT.2020.3026314.
[77] Y. Zhao et al., "Multi-channel WDM (de)multiplexer based on multimode contra-directional coupling using dielectric etches," in *Proc. Asia Commun. Photon. Conf./Int. Conf. Inf. Photon. Opt. Commun.*, 2020, Art. no. M4A.178, doi: 10.1364/ACPC.2020.M4A.178.
[78] Y. Zheng et al., "Design of 4-channel AWG multiplexer/demultiplexer for CWDM system," *Optik*, vol. 201, Jan. 2020, Art. no. 163513, doi: 10.1016/j.ijleo.2019.163513.
[79] E. Zubkova et al., "CWDM demultiplexer using anti-reflection, contra-directional couplers based on silicon nitride rib waveguide," *J. Phys. Conf. Ser.*, vol. 1410, no. 1, Dec. 2019, Art. no. 012179, doi: 10.1088/1742-6596/1410/1/012179.
[80] J.-H. Jung, "Optimization for arrayed waveguide grating having MMI coupler for flattened transfer function," *J. Opt. Soc. Korea*, vol. 10, no. 4, pp. 169–173, Dec. 2006.
[81] K. Okamoto and H. Yamada, "Arrayed-waveguide grating multiplexer with flat spectral response," *Opt. Lett.*, vol. 20, no. 1, pp. 43–45, Jan. 1995, doi: 10.1364/OL.20.000043.
[82] S. Pathak et al., "Compact SOI-based AWG with flattened spectral response using a MMI," in *Proc. 8th IEEE Int. Conf. Group IV Photon.*, 2011, pp. 45–47, doi: 10.1109/GROUP4.2011.6053710.
[83] S. Pathak et al., "Optimized silicon AWG with flattened spectral response using an MMI aperture," *J. Lightw. Technol.*, vol. 31, no. 1, pp. 87–93, Jan. 2013, doi: 10.1109/JLT.2012.2231399.
[84] R. Kashyap, *Fiber Bragg gratings / Raman Kashyap*, 2nd ed. Burlington, MA, USA: Academic Press, Oct. 2009.
[85] Z. Zhan et al., "Adaptive particle swarm optimization," *IEEE Trans. Syst. Man, Cybern. Part B (Cybern.)*, vol. 39, no. 6, pp. 1362–1381, Dec. 2009, doi: 10.1109/TSMCB.2009.2015956.
[86] S. Pathak et al., "Comparison of AWGs and echelle gratings for wavelength division multiplexing on silicon-on-insulator," *IEEE Photon. J.*, vol. 6, no. 5, Oct. 2014, Art. no. 4900109, doi: 10.1109/JPHOT.2014.2361658.